REVIEW OF SCIENTIFIC INSTRUMENTS **87**, 053707 (2016)

Development of a spectroscopic Mueller matrix imaging ellipsometer for nanostructure metrology

Xiuguo Chen,[1] Weichao Du,[1] Kui Yuan,[1] Jun Chen,[1] Hao Jiang,[1,a)] Chuanwei Zhang,[1,2] and Shiyuan Liu[1,2,a)]
[1]*State Key Laboratory of Digital Manufacturing Equipment and Technology, Huazhong University of Science and Technology, Wuhan 430074, China*
[2]*Wuhan Eoptics Technology Co. Ltd., Wuhan 430075, China*

(Received 26 September 2015; accepted 9 May 2016; published online 31 May 2016)

In this paper, we describe the development of a spectroscopic Mueller matrix imaging ellipsometer (MMIE), which combines the great power of Mueller matrix ellipsometry with the high spatial resolution of optical microscopy. A dual rotating-compensator configuration is adopted to collect the full 4×4 imaging Mueller matrix in a single measurement. The light wavelengths are scanned in the range of 400–700 nm by a monochromator. The instrument has measurement accuracy and precision better than 0.01 for all the Mueller matrix elements in both the whole image and the whole spectral range. The instrument was then applied for the measurement of nanostructures combined with an inverse diffraction problem solving technique. The experiment performed on a photoresist grating sample has demonstrated the great potential of MMIE for accurate grating reconstruction from spectral data collected by a single pixel of the camera and for efficient quantification of geometrical profile of the grating structure over a large area with pixel resolution. It is expected that MMIE will be a powerful tool for nanostructure metrology in future high-volume nanomanufacturing. *Published by AIP Publishing.* [http://dx.doi.org/10.1063/1.4952385]

I. INTRODUCTION

Ellipsometry is an optical metrology technique that utilizes polarized light to characterize thickness of thin films and optical constants of both layered and bulk materials.[1,2] Since the year of around 2000, spectroscopic ellipsometry was introduced to monitor critical dimension of grating structures in semiconductor manufacturing.[3,4] Compared with scanning electron microscopy (SEM) and atomic force microscopy (AFM), this technique, also referred to as optical scatterometry or optical critical dimension metrology, has achieved wide industrial applications after decades of development due to its attractive advantages, such as low cost, high throughput, and minimal sample damage. Among the various types of ellipsometers, Mueller matrix ellipsometer (MME), also known as Mueller matrix polarimeter, can provide all 16 elements of a 4×4 Mueller matrix. Consequently, MME-based scatterometry can acquire much more useful information about the sample, such as anisotropy and depolarization, and thereby can achieve better measurement sensitivity and accuracy.[5–10] Usually, scatterometric measurements are carried out on special target gratings etched in scribe lines between chips with the size of the illumination spot smaller than that of the grating target. Standard spot sizes are in the range from 3 to 1 mm in diameter, and microspot sizes, depending on the spectral range of measurements, are typically between 50 and 25 μm so far.[11] Smaller microspots are highly desirable but will greatly complicate the optical system. In addition, if the lateral distribution of optical properties and geometrical profile of a sample surface is of interest, scatterometric measurements are usually carried out point-by-point by mechanical scanning techniques. This is normally not a practical solution as such a scan takes quite a long time.

In this work, we address the above inherent issues in scatterometry techniques and present the development of a spectroscopic Mueller matrix imaging ellipsometer (MMIE), which enables ellipsometric analysis with pixel-sized illumination spot and quantification of geometrical profile distribution of nanostructures without scanning the sample stage. Imaging ellipsometry is a hybrid of ellipsometry and optical microscopy, which combines the high thickness sensitivity of ellipsometry with the high spatial resolution of optical microscopy. Imaging ellipsometry techniques first emerged in the 1980′, which were developed for quantitative measurements and analysis of film thickness uniformity in semiconductor integrated circuit processing.[12–16] Over the past decades, many types of imaging ellipsometers have been developed by combining imaging techniques with different ellipsometers, such as the null ellipsometer,[12,13] the rotating analyzer ellipsometer,[14] the rotating compensator ellipsometer,[15] and also the Mueller matrix ellipsometer.[17–19] In the meanwhile, a few applications of imaging ellipsometry have also appeared. These applications are typically concentrated on two aspects to the best of our knowledge. The first aspect is the characterization of all kinds of nanofilms formed on surfaces and interfaces, such as the characterization of monomolecular layers,[20] self-assembled monolayers,[21] graphene,[22] and thin-film photovoltaics.[23] Another aspect is the application in biomedicine for the diagnosis and monitoring of human diseases, such as the retinal disease[24] and cancers.[25,26] This work expands the application of imaging ellipsometry for the

a)Authors to whom correspondence should be addressed. Electronic addresses: hjiang@hust.edu.cn (H. Jiang) and shyliu@hust.edu.cn (S. Liu)

Reuse of AIP Publishing content is subject to the terms at: https://publishing.aip.org/authors/rights-and-permissions. Download to IP: 115.156.193.89 On: Wed, 15 Jun 2016 09:24:26

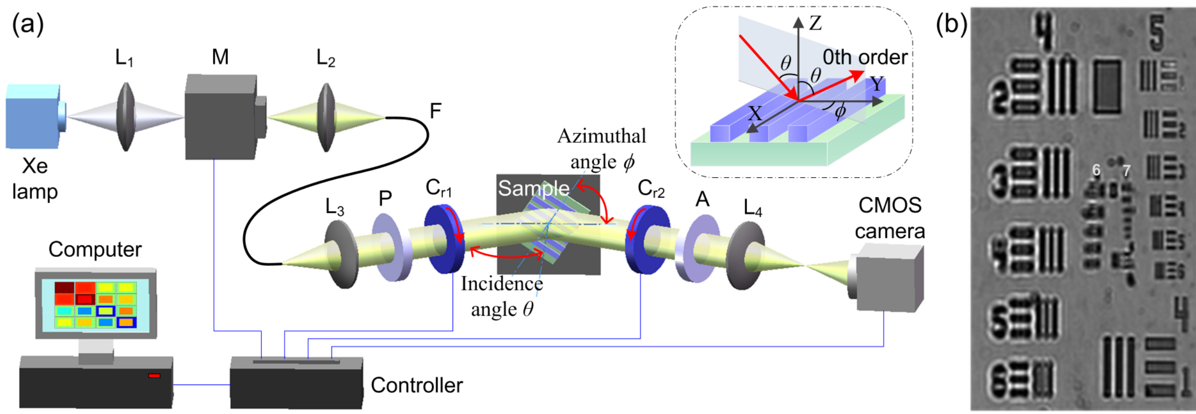

FIG. 1. (a) The schematic diagram of the dual rotating-compensator MMIE. L_1 and L_2, focusing lens; M, monochromator; F, fiber; L_3, collimating lens; P and A, polarizer and analyzer; C_{r1} and C_{r2}, the 1st and 2nd rotating compensator; L_4, imaging lens. The upper right image presents the scheme of a light beam incidence upon a one-dimensional grating structure with the incidence angle of θ and azimuthal angle of ϕ; (b) test pattern taken by the MMIE at the wavelength of 500 nm without the polarization elements.

measurement of nanostructures in combination with an inverse diffraction problem solving technique.

The remainder of this paper is organized as follows. Section II introduces the design, operation principle, and calibration of an in-house developed spectroscopic MMIE. Section III introduces the data analysis for nanostructure reconstruction from the MMIE-measured spectra. Section IV provides the corresponding experimental results to demonstrate the performance of the developed instrument as well as its great potential in nanostructure metrology. Finally, we draw some conclusions and show the outlook of the present technique in Section V.

II. INSTRUMENTATION

A. Operation principle

A dual rotating-compensator configuration is adopted to measure the sample imaging Mueller matrix. As shown in Fig. 1(a), an expanded parallel beam generated by a collimating lens illuminates a sample and the reflected light intensity is measured by a polarization blind camera. The basic system layout of the dual rotating-compensator MMIE in order of light propagation is $\mathrm{PC_{r1}}(\omega_1)\mathrm{SC_{r2}}(\omega_2)\mathrm{A}$, where P and A stand for the fixed polarizer and analyzer, $\mathrm{C_{r1}}$ and $\mathrm{C_{r2}}$ refer to the 1st and 2nd rotating compensators, and S stands for the sample. The 1st and 2nd compensators rotate synchronously at $\omega_1 = 5\omega$ and $\omega_2 = 3\omega$, where ω is the fundamental mechanical frequency. The emerging Stokes vector $\mathbf{S}_{\mathrm{out}}$ at every pixel of the camera can be expressed as the following Mueller matrix product[10,27]

$$\mathbf{S}_{\mathrm{out}} = [\mathbf{M}_{\mathrm{A}}\mathbf{R}(A)][\mathbf{R}(-C_2)\mathbf{M}_{\mathrm{C2}}(\delta_2)\mathbf{R}(C_2)]\mathbf{M}_{\mathrm{S}} \times [\mathbf{R}(-C_1)\mathbf{M}_{\mathrm{C1}}(\delta_1)\mathbf{R}(C_1)][\mathbf{R}(-P)\mathbf{M}_{\mathrm{P}}\mathbf{R}(P)]\mathbf{S}_{\mathrm{in}}, \quad (1)$$

where $\mathbf{M}_i$ (i = P, A, C1, C2, S) is the Mueller matrix associated with each optical element and the sample. $\mathbf{R}(\alpha)$ is the Mueller rotation transformation matrix for rotation by an angle α, which can be the transmission-axis orientations of the polarizer and analyzer, P and A, and the fast-axis orientations of the 1st and 2nd rotating compensators, C_1 and C_2. Here, $C_1 = \omega_1 t + C_{\mathrm{S1}}$ and $C_2 = \omega_2 t + C_{\mathrm{S2}}$, and C_{S1} and C_{S2} represent the initial fast-axis positions of the two compensators. δ_1 and δ_2 are the phase retardances of the 1st and 2nd compensators. By multiplying the matrices in Eq. (1), we obtain the following expression for the irradiance at every pixel of the camera (proportional to the first element of $\mathbf{S}_{\mathrm{out}}$)

$$\begin{aligned} I(t) &= I_{00}M_{11}\left\{a_0 + \sum_{n=1}^{16}[a_{2n}\cos(2n\omega t - \phi_{2n}) + b_{2n}\sin(2n\omega t - \phi_{2n})]\right\} \\ &= I_0\left\{1 + \sum_{n=1}^{16}[\alpha_{2n}\cos(2n\omega t - \phi_{2n}) + \beta_{2n}\sin(2n\omega t - \phi_{2n})]\right\}, \end{aligned} \quad (2)$$

where I_{00} is the spectral response function and ϕ_{2n} is the angular phase shift. $I_0 = I_{00}M_{11}a_0$, $\alpha_{2n} = a_{2n}/a_0$, and $\beta_{2n} = b_{2n}/a_0$ are the d.c. and normalized a.c. harmonic coefficients, respectively. The sample Mueller matrix elements M_{ij} (i, j = 1, 2, 3, 4) are linear combinations of α_{2n} and β_{2n}. Further details about the relation between M_{ij} and α_{2n} and β_{2n} can be found in Ref. 27.

The irradiance measured at every pixel of the camera in a dual rotating-compensator system obeys the following experimental expression

$$I(t) = I_0'\left[1 + \sum_{n=1}^{16}(\alpha_{2n}'\cos 2n\omega t + \beta_{2n}'\sin 2n\omega t)\right], \quad (3)$$

where

Reuse of AIP Publishing content is subject to the terms at: https://publishing.aip.org/authors/rights-and-permissions. Download to IP: 115.156.193.89 On: Wed, 15 Jun 2016 09:24:26

$$I_0' = I_0, \tag{4a}$$

$$[\alpha_{2n}, \beta_{2n}]^{\mathrm{T}} = \Re(\phi_{2n})[\alpha'_{2n}, \beta'_{2n}]^{\mathrm{T}}, \tag{4b}$$

the superscript "T" represents the matrix transpose and $\Re(\phi_{2n})$ is a 2×2 rotation transformation matrix. To detect the waveform given in Eq. (3), one can perform K times the number of integrals of the irradiance over the fundamental optical period of π/ω, which leads to raw flux data $\{g_k,\ k = 1,\ 2,\ \ldots,\ K\}$ of the form

$$\begin{aligned} g_k &= \int_{(k-1)\pi/K\omega}^{k\pi/K\omega} I_0' \left[1 + \sum_{n=1}^{16} \left(\alpha'_{2n}\cos 2n\omega t + \beta'_{2n}\sin 2n\omega t\right)\right] dt \\ &= \frac{\pi I_0'}{K\omega} + \sum_{n=1}^{16} \frac{I_0'}{n\omega}\left(\sin\frac{n\pi}{K}\right)\left[\alpha'_{2n}\cos\frac{(2k-1)n\pi}{K} + \beta'_{2n}\sin\frac{(2k-1)n\pi}{K}\right]. \end{aligned} \tag{5}$$

Since the harmonic coefficients $\{(\alpha'_{2n},\ \beta'_{2n}),\ n = 9,\ 12,\ 14,\ 15\}$ all vanish, there are only 25 unknowns in Eq. (5), including 24 nonzero harmonic coefficients along with I_0'. Since the highest-order nonzero harmonic coefficient is at $32\omega t$, according to the Nyquist sampling theorem, at least $K \geq 33$ integrations over the fundamental optical cycle (π/ω) are required to extract the harmonic coefficients $\{(I_0', \alpha'_{2n}, \beta'_{2n}),\ n = 1,2,\ldots,8,10,11,13,16\}$ by Eq. (5). According to Eq. (4), we can further obtain the harmonic coefficients $\{I_0, \alpha_{2n}, \beta_{2n}\}$, from which we can finally obtain the sample Mueller matrix elements $M_{ij}\ (i,j = 1,2,3,4)$ associated with every pixel of the camera. All the Mueller matrices associated with every pixel of the camera compose the sample imaging Mueller matrix.

From Eqs. (2)-(5), we know that the relation between the sample Mueller matrix elements M_{ij} and the measured fluxes g_k is essentially a linear transformation, which can be simply formulated as

$$\mathbf{G} = \mathbf{D}\cdot\mathbf{m}, \tag{6}$$

where $\mathbf{G}$ is a $K\times 1$ flux vector with the k-th element being g_k, $\mathbf{m}$ is a 16×1 Mueller vector obtained by reading the sample Mueller matrix elements in a lexicographic order, i.e., $\mathbf{m} = [M_{11}, M_{12}, M_{13}, M_{14}, M_{21}, M_{22}, \ldots, M_{44}]^{\mathrm{T}}$, and $\mathbf{D}$ is a $K\times 16$ instrument matrix. According to Eq. (6), the sample Mueller matrix can also be obtained by

$$\mathbf{m} = \mathbf{D}^{+}\cdot\mathbf{G}, \tag{7}$$

where $\mathbf{D}^{+} = (\mathbf{D}^{\mathrm{T}}\mathbf{D})^{-1}\mathbf{D}^{\mathrm{T}}$ is the Moore-Penrose pseudo-inverse of the matrix $\mathbf{D}$. In addition, we can use the condition number of $\mathbf{D}$ defined by

$$\mathrm{cond}(\mathbf{D}) = \|\mathbf{D}\|\ \|\mathbf{D}^{+}\|, \tag{8}$$

as a metric for optimizing MMIE to minimize the effect of small errors in $\mathbf{G}$ and $\mathbf{D}$ on $\mathbf{m}$. The notation $\|\cdot\|$ in Eq. (8) denotes the maximum norm of a matrix.[28] The system parameters that need to be optimized include the transmission-axis orientations P and A of the polarizer and analyzer, the retardances δ_1 and δ_2 and initial fast-axis orientations C_{S1} and C_{S2} of the two compensators.

B. Instrument description

In the developed dual rotating-compensator MMIE, the light beam from a laser-driven light source (LDLS™ Eq-99XFC, Energetiq Technology, Inc., USA) goes successively through an achromatic lens pair (MAP105050-A, Thorlabs, Inc., USA) and a monochromator (Omni-λ320i, Zolix Instruments Co., Ltd, China) to select the wavelength of measurements. The light beam from the monochromator passes through another achromatic lens pair (MAP107575-A, Thorlabs, Inc., USA) and then focuses on one side of a fiber (FRS-400-0.22-1.5-BB-SW, B&W Tek, Inc., USA). The fiber, in a slit-to-round configuration, changes the rectangular light beam exiting from the monochromator into a circular one to reduce the intensity loss. The exiting light beam from the round side of the fiber becomes an expanded parallel beam after passing through a collimating lens (AC254-100-A-ML, Thorlabs, Inc., USA). The parallel light beam passes successively through the polarizer, the 1st rotating compensator, and is reflected from the sample surface, and then through the 2nd rotating compensator, the analyzer, an imaging lens, and finally goes into a camera. The polarizer (analyzer) is a α-BBO Glan-Taylor polarizer with an extinction ratio of less than 5×10^{-6} (PGT6312, Union Optic, Inc., China). The compensator (the 1st and 2nd rotating compensators) is an optimally designed achromatic Quartz biplate that consists of two zero-order quarter Quartz waveplates and is mounted in a hollow-shaft servo-motor (HO-63-A-E-000, Applimotion, Inc., USA). The imaging lens comprises double achromatic lenses (AC254-200-A-ML, Thorlabs, Inc., USA) and has a focal length and an image magnification of 200 mm and 1:1, respectively. The camera is an industrial camera with a CMOS global shutter sensor (Manta G-235B/C, Applied Vision Technology, Inc., Germany). It has 1936×1216 pixels with each pixel size of $5.86\times 5.86\ \mu\mathrm{m}^2$. To obtain a clear image of the entire sample surface, the camera was mounted with a slight tilt with respect to the optical axis. All the achromatic lenses from Thorlabs, Inc., have anti-reflective coatings for the 400–700 nm wavelength range.

In the optimization of the Quartz biplate, the associated phase retardance is represented as a function of three parameters, i.e., the two central wavelengths of the constituent zero-order quarter waveplates as well as the angle between fast axes of the two waveplates.[29] These three parameters together with other system parameters are then optimized by minimizing the condition number of $\mathbf{D}$ given in Eq. (8) over the spectral of 400–700 nm. The 1st and 2nd compensators rotate synchronously at $\omega_1 = 5\pi$ rad/s (2.5 Hz) and

Reuse of AIP Publishing content is subject to the terms at: https://publishing.aip.org/authors/rights-and-permissions. Download to IP: 115.156.193.89 On: Wed, 15 Jun 2016 09:24:26

$\omega_2 = 3\pi$ rad/s (1.5 Hz), respectively, which are controlled by a programmable multi-axis controller (Delta Tau Data Systems Inc., USA). To detect the waveform given in Eq. (3), we set the integration time as ~20 ms and perform $K = 50$ times the number of integrals of the irradiance over the fundamental optical period (π/ω). We can thereby know that the camera acquires images at ~50 fps (frames per second). In addition, the measured flux data g_k (see Eq. (5)) are averaged over 10 fundamental optical periods to improve the signal-to-noise ratio. Thus, the imaging Mueller matrix measurement at a single wavelength will take ~10 s, and the measurement for imaging Mueller matrices in the whole spectral range of 400–700 nm with increments of 10 nm will take ~5 min.

It is worth pointing out that the present technique in this work for nanostructure metrology is essentially identical to typical optical scatterometry techniques, in which only the zeroth order diffracted light of a periodic nanostructure is collected by the camera, as depicted in Fig. 1(a). When high order diffracted light beams enter into the camera, clear structure images will be observed. In this case, the structural features can be directly obtained from the acquired images by proper image recognition algorithms,[30] as do in conventional image-based metrology techniques, without solving the inverse diffraction problem. It is thereby beyond the scope of this work. In the developed MMIE, the numerical aperture (NA) of the imaging lens is ~0.062. Moreover, due to the limitation of the clear aperture (~9.5 mm) of the compensator in the instrument, the effective NA of the imaging lens will be much smaller (~0.024), which ensures that only the zeroth order diffracted light is collected for nanostructures below the wavelength scale.

A test chart comprising a series of horizontal and vertical lines (1951 USAF resolution test target, Thorlabs, Inc., USA) was used to estimate the lateral resolution of the developed MMIE. A set of six elements (horizontal and vertical line pairs) are in one group, and six groups (from Group 2 to Group 7) compose the resolution chart. The spacing between the lines in each element is equal to the width of the line itself. When the target is imaged, the resolution of an imaging system can be estimated by viewing the clarity of the horizontal and vertical lines. Figure 1(b) shows the image of Groups 4 to 7 taken by the MMIE at the wavelength of 500 nm. In the measurement, the polarizer, the analyzer, and the two rotating compensators were removed from the instrument so that they did not affect the test result. As shown in Fig. 1(b), the largest set of distinguishable horizontal and vertical lines corresponds to Element 3 of Group 5 on the resolution target, which indicates that the maximum resolution is 40.3 line pairs per millimeter (equates to ~24.8 μm per line pairs).

C. Instrument calibration

The objective of the calibration is determination of the actual transmission-axis orientations P and A of the polarizer and analyzer, the initial fast-axis orientations C_{S1} and C_{S2} of the two compensators as well as their wavelength-dependent phase retardances δ_1 and δ_2. We use a regression method to obtain the calibration values of P, A, C_{S1}, C_{S2}, δ_1 and δ_2. To implement the regression calibration, normalized harmonic coefficients are first measured according to Eqs. (4) and (5), which are denoted as $\alpha_{2n}^{\exp}$ and $\beta_{2n}^{\exp}$. Data calculated for a calibration sample from Eqs. (1) and (2), denoted as $\alpha_{2n}^{\text{calc}}(P, A, C_{S1}, C_{S2}, \delta_1, \delta_2)$ and $\beta_{2n}^{\text{calc}}(P, A, C_{S1}, C_{S2}, \delta_1, \delta_2)$, are then fitted to the experimental data wavelength-by-wavelength by adjusting the parameters P, A, C_{S1}, C_{S2}, δ_1 and δ_2 to minimize a χ^2 error function defined by

$$\chi^2 = \sum_{n=1}^{16} \left\{ \left[\frac{\alpha_{2n}^{\exp} - \alpha_{2n}^{\text{calc}}(P, A, C_{S1}, C_{S2}, \delta_1, \delta_2)}{\sigma(\alpha_{2n})} \right]^2 + \left[\frac{\beta_{2n}^{\exp} - \beta_{2n}^{\text{calc}}(P, A, C_{S1}, C_{S2}, \delta_1, \delta_2)}{\sigma(\beta_{2n})} \right]^2 \right\}, \quad (9)$$

where $\sigma(\alpha_{2n})$ and $\sigma(\beta_{2n})$ are the standard deviations of the experimental harmonic coefficients measured at the corresponding spectral point. Minimizing χ^2 is done by an iterative non-linear regression analysis, such as the Levenberg-Marquardt algorithm.[31] From the regression method, the system parameters P, A, C_{S1}, C_{S2}, δ_1 and δ_2 in the whole measured spectral range can be determined. We can then further parameterize the calibration parameters, especially the phase retardances δ_1 and δ_2, using proper dielectric function models. According to the parameterized model, we may perform a similar χ^2 fitting procedure illustrated above for the whole spectral range again to determine the calibration parameters more accurately. In addition, to reduce the effect of nonuniformity of light intensity, the regression calibration is first performed for every pixel of the camera separately, and then the achieved calibration parameters are averaged over all the pixels.

III. DATA ANALYSIS

The reconstruction of the nanostructure profile from MMIE-measured spectra is a typical inverse diffraction problem with the objective of finding a profile whose theoretical spectra can best match the measured spectra. Theoretical Mueller matrices of a periodic nanostructure can be calculated by the rigorous coupled-wave analysis (RCWA).[32–34] In RCWA, both the permittivity function and electromagnetic fields are expanded into Fourier series. Afterwards, the tangential filed components are matched at boundaries between different layers, and thereby the boundary-value problem is reduced to an algebraic eigenvalue problem. The overall reflection coefficients can be calculated by solving this eigenvalue problem. According to the reflection coefficients, the 2×2 Jones matrix $\mathbf{J}$ associated with the zeroth order diffracted light of the sample, which connects the incoming Jones vector with the diffracted one, can be formulated by

$$\begin{bmatrix} E_{\text{rp}} \\ E_{\text{rs}} \end{bmatrix} = \mathbf{J} \begin{bmatrix} E_{\text{ip}} \\ E_{\text{is}} \end{bmatrix} = \begin{bmatrix} r_{\text{pp}} & r_{\text{ps}} \\ r_{\text{sp}} & r_{\text{ss}} \end{bmatrix} \begin{bmatrix} E_{\text{ip}} \\ E_{\text{is}} \end{bmatrix}, \quad (10)$$

where $E_{\text{s,p}}$ refers to the electric field component perpendicular and parallel to the plane of incidence, respectively. In the absence of depolarization, the 4×4 Mueller matrix $\mathbf{M}$ can be

Reuse of AIP Publishing content is subject to the terms at: https://publishing.aip.org/authors/rights-and-permissions. Download to IP: 115.156.193.89 On: Wed, 15 Jun 2016 09:24:26

calculated from the Jones matrix $\mathbf{J}$ by[1]

$$\mathbf{M} = \mathbf{A}(\mathbf{J} \otimes \mathbf{J}^*)\mathbf{A}^{-1}, \tag{11a}$$

where the symbol $\otimes$ denotes the Kronecker product, $\mathbf{J}^*$ is the complex conjugate of $\mathbf{J}$, and the matrix $\mathbf{A}$ is given by

$$\mathbf{A} = \begin{bmatrix} 1 & 0 & 0 & 1 \\ 1 & 0 & 0 & -1 \\ 0 & 1 & 1 & 0 \\ 0 & \mathrm{i} & -\mathrm{i} & 0 \end{bmatrix}. \tag{11b}$$

In practice, the Mueller matrix $\mathbf{M}$ is usually normalized to the (1, 1)th element M_{11}, with the normalized Mueller matrix elements being $m_{ij} = M_{ij}/M_{11}$.

A weighted least-squares regression analysis (Levenberg-Marquardt algorithm) is then performed for any pixel of the MMIE camera, during which the structural parameters under measurement are varied until the calculated and measured data match as close as possible. This is done by minimizing a weighted mean square error function χ_r^2 defined by

$$\chi_r^2 = \frac{1}{15N - P} \sum_{k=1}^{N} \sum_{j=1}^{4} \left[\frac{m_{ij,k}^{\text{exp}} - m_{ij,k}^{\text{calc}}(\mathbf{x})}{\sigma(m_{ij,k})} \right]^2, \tag{12}$$

where k indicates the kth spectral point from the total number N, indices i and j show all the Mueller matrix elements except m_{11} (normalized to m_{11}), $\mathbf{x}$ is a P-dimensional vector consists of the structural parameters under measurement, $m_{ij,k}^{\text{exp}}$ denotes the Mueller matrix elements measured by the current pixel of the camera with the standard deviation of $\sigma(m_{ij,k})$, and $m_{ij,k}^{\text{calc}}(\text{x})$ denotes the calculated Mueller matrix elements associated with the vector $\mathbf{x}$. The fitting procedure delivers 95% confidence limits of $1.96 \times \chi_r \times \sqrt{C_{ii}}$ for the structural parameters, where C_{ii} is the ith diagonal element of the structural parameter covariance.[35] The regression analysis is mostly applied for the analysis of data collected by a single pixel or a number of pixels, while might be unsuitable for data analysis of a large area (usually contain millions of pixels that need to be processed) due to the intensive RCWA calculation. In this case, the library search method can be applied,[36] where a Mueller matrix spectra library is generated prior to the measurement and then the library is searched to find the best match with the measured spectra. Although the offline generation of the spectra library is time-consuming, the search itself during the online measurement can be done quickly with a global solution guaranteed.

IV. MEASUREMENT

A. Sample description

As shown in Fig. 2(a), the investigated sample is an 8 inch Si wafer that contains 25 identical dies, and the magnified image of one die is presented in Fig. 2(b) for demonstration. The rectangle-marked region on this magnified image, also termed as the metrological box in the remainder of the paper, has a size of about 3×2.5 mm^2 and consists of a photoresist array on a bottom anti-reflective coating (BARC) layer deposited on a Si substrate. The photoresist grating structure was fabricated using a 193 nm wavelength lithography tool, with a well-designed BARC layer to avoid standing waves in the photoresist. Figure 2(c) shows the cross-sectional SEM (Nova NanoSEM450, FEI Co., USA) micrograph of the photoresist grating structure as well as the adopted geometrical model to characterize its line shape. As shown in Fig. 2(c), the geometrical profile of the photoresist grating is characterized by top critical dimension x_1, sidewall angle x_2, and grating height x_3. The thickness of the BARC layer is represented by x_4. The period of the photoresist grating is 400 nm. The nominal dimensions of structural parameters of the grating sample are: $x_1 = 200$ nm, $x_2 = 90°$, $x_3 = 311$ nm, and $x_4 = 115$ nm, respectively. In the data analysis, the optical constants of the Si substrate were fixed at values taken from the literature.[37] The optical properties of the BARC layer were modeled using a two-term Forouhi-Bloomer model,[38] whose parameters were predetermined from a BARC film deposited on the Si substrate using a ME-L spectroscopic ellipsometer (Wuhan EOptics Technology Co., China). The ME-L ellipsometer is a high-precision MME, which can provide full 4×4 Mueller matrices in the spectral range of 200–1000 nm.[10] The parameters of the two-term Forouhi-Bloomer model were taken as $A_1 = 6.029 \times 10^{-3}$, $A_2 = 2.060 \times 10^{-2}$, $B_1 = 14.1953$ eV, $B_2 = 14.1964$ eV, $C_1 = 50.5239$ eV^2, $C_2 = 50.5379$ eV^2, $n(\infty) = 1.4361$, and $E_g = 4.7741$ eV, respectively. The optical properties of the photoresist were modeled using a Tauc-Lorentz model,[39] whose parameters were predetermined from a photoresist film deposited on the Si substrate using the same MME and taken as $\varepsilon_\infty = 1.4268$, $E_g = 3.4597$ eV, $A = 21.1496$ eV, $C = 0.9877$ eV, and $E_0 = 9.9492$ eV, respectively.

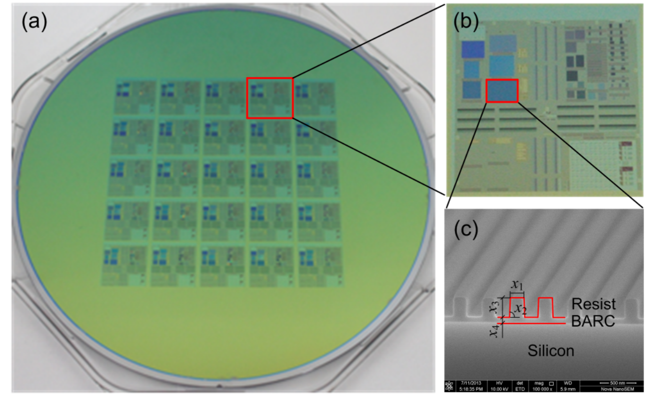

FIG. 2. (a) The photograph of the Si wafer; (b) the magnified image of one die that corresponds to the rectangle-marked region on the image of the Si wafer, and the rectangle-marked region on the magnified image corresponds to the metrological box where the photoresist grating structure is; (c) the cross-sectional SEM micrograph and geometric model of the photoresist grating structure.

B. Results and discussion

Prior to the measurement, the developed MMIE was first calibrated in a reflection setup using a 25 nm SiO_2/Si standard sample and in a transmission setup without placing the sample (namely taking air as the sample). Repeated measurements were then performed for air, whose theoretical Mueller matrix

Reuse of AIP Publishing content is subject to the terms at: https://publishing.aip.org/authors/rights-and-permissions. Download to IP: 115.156.193.89 On: Wed, 15 Jun 2016 09:24:26

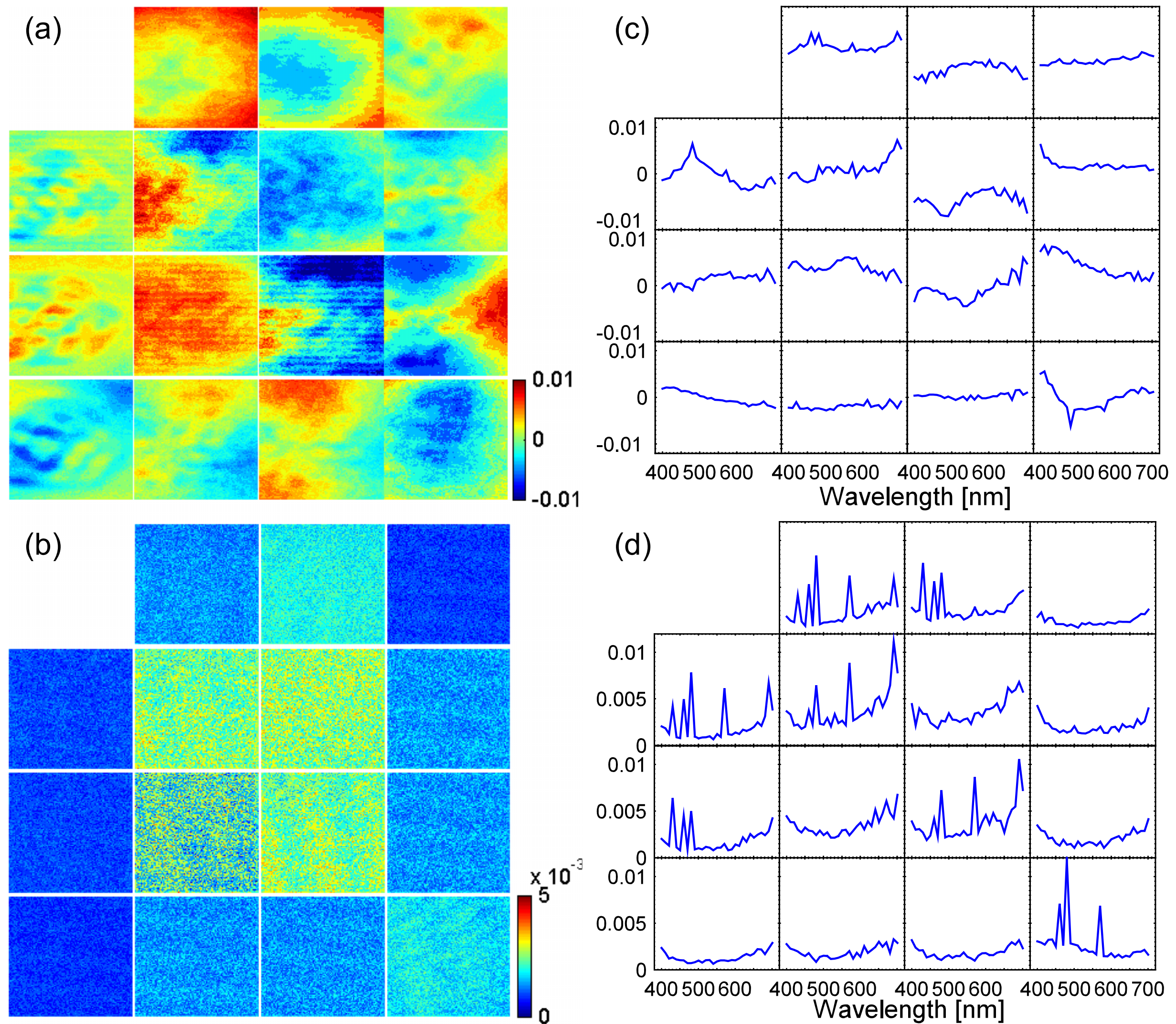

FIG. 3. (a) Mean bias and (b) standard deviation of the imaging Mueller matrix of air measured over a square area of about 4×4 mm^2 at the wavelength of 550 nm, (c) Mean bias and (d) standard deviation of the spectral Mueller matrix of air collected by a single pixel of the camera. The mean bias and standard deviation are estimated by 30 repeated measurements.

is a 4×4 identity matrix at any wavelength, to evaluate the performance of the developed instrument. Figures 3(a) and 3(b) present the mean bias and standard deviation of the imaging Mueller matrix of air measured over a square area of about 4×4 mm^2 at the wavelength of 550 nm for illustration. The bias of the Mueller matrix is defined as the difference between the measured and theoretical Mueller matrices. As can be observed from Figs. 3(a) and 3(b), the absolute mean bias and standard deviation of the measured imaging Mueller matrix are less than 0.01 and 0.005, respectively, in the whole image area. Figures 3(c) and 3(d) present the mean bias and standard deviation of the spectral Mueller matrix of air collected by a randomly selected pixel of the MMIE camera. As can be observed, the absolute mean bias and standard deviation of the measured spectral Mueller matrix are less than 0.01 and 0.015, respectively, in the whole spectral range of 400–700 nm.

To further verify the absolute accuracy of the MMIE measurement, we also compared it with the above-mentioned MME (ME-L ellipsometer). For this experiment, five SiO_2/Si standard samples with nominal oxide layer thicknesses of 2 nm, 10 nm, 25 nm, 340 nm, and 1000 nm, respectively, were measured by both the MMIE and MME at the incidence angle of 60° and in the spectral range of 400–700 nm. The measurement for each sample was taken at the centre of the sample. The beam spot size of the MME is about 3 mm. For comparison, the MMIE-measured data were properly averaged over 3 mm measurement site. The results are presented in Table I and show excellent agreement between the measurements.

TABLE I. Comparison of oxide layer thicknesses of SiO_2/Si standard samples extracted from MMIE and MME measurements at the incidence angle of 60° and in the spectral range of 400–700 nm.

Film sample no.	MMIE (thickness, nm)	MME (thickness, nm)
1	1.9	1.8
2	10.9	10.9
3	22.3	22.1
4	341.0	341.7
5	1026.8	1028.3

Reuse of AIP Publishing content is subject to the terms at: https://publishing.aip.org/authors/rights-and-permissions. Download to IP: 115.156.193.89 On: Wed, 15 Jun 2016 09:24:26

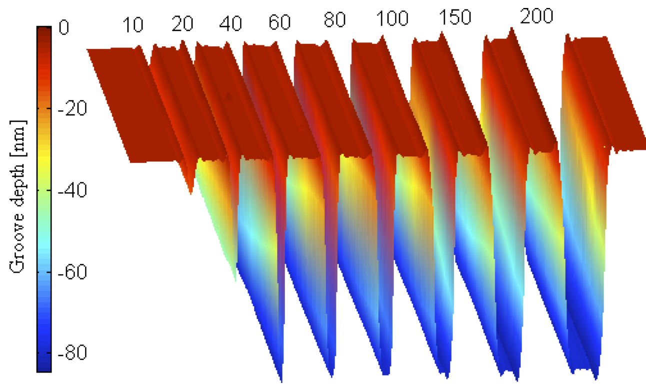

FIG. 4. Reconstructed map of parallel grooves with different widths in a SiO_2 layer on a Si substrate. The number at each groove with a unit of micrometer represents the width of the groove.

To further test the lateral resolution of the developed MMIE, a sample was prepared with 8 parallel grooves of different widths etched in a SiO_2 layer on a Si substrate. The nominal widths of the 8 parallel grooves are 10 μm, 20 μm, 40 μm, 60 μm, 80 μm, 100 μm, 150 μm and 200 μm, respectively. We measured their actual widths using a profilometer (KLA Tencor P16+) and found that the maximum absolute error between the actual and nominal widths of these grooves is less than 1 μm. All the grooves have the same depth of about 80 nm. The interval between any two adjacent grooves is about 200 μm. Figure 4 shows the reconstructed map of the grooves. As can be observed from Fig. 4, the grooves with widths of 10 μm and 20 μm cannot be distinguished, which indicates that the lateral resolution is worse than 20 μm. In the meanwhile, the grooves with widths of 40 μm and 60 μm can be visualized with at least one pixel and two pixels, respectively, which means that the lateral resolution is better than 30 μm. The test result is thus in accordance with that achieved by a test chart presented at the end of the Section II B.

The photoresist grating sample was then measured using the MMIE. In the measurement, the incidence and azimuthal angles were fixed at $\theta = 60°$ and $\phi = 0°$, respectively. As an example, Fig. 5 shows the imaging Mueller matrix measured over an area of about 3.9×3.3 mm^2 on the sample at the wavelength of 500 nm. At the azimuthal angle of $\phi = 0°$, i.e., with the plane of incidence perpendicular to grating lines, the two 2×2 off-diagonal blocks of the Mueller matrices vanish, as can be observed from Fig. 5, while other elements can be expressed in terms of conventional ellipsometric angles Ψ and Δ,[1,2] i.e., $m_{12} = m_{21} = -\cos 2\Psi$, $m_{34} = -m_{43} = \sin 2\Psi \sin \Delta$, and $m_{33} = m_{44} = \sin 2\Psi \cos \Delta$ ($m_{11} = m_{22} = 1$). Since only the zeroth order diffracted light of the photoresist grating is collected, we will not obtain the image of its structural features. However, due to the difference (or contrast) between Mueller matrices associated with different regions, we can readily distinguish the metrological box where the photoresist grating is from the presented imaging Mueller matrix in Fig. 5. According to the measured imaging Mueller matrices, we can intuitively choose the region or pixels of interest for further ellipsometric analysis to reconstruct the geometrical profile of the photoresist grating structure.

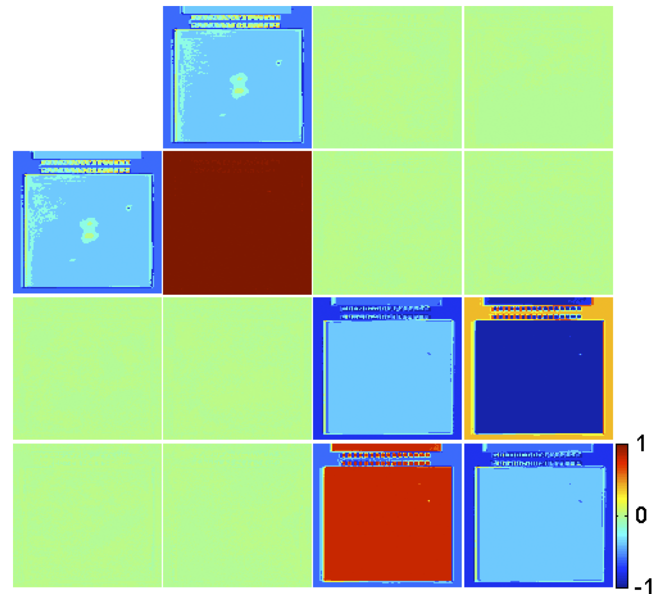

FIG. 5. The imaging Mueller matrix (normalized to m_{11}, which is not shown) of the photoresist grating sample measured over an area of about 3.9×3.3 mm^2 on the sample at the wavelength of 500 nm. The central rectangular region shown in the Mueller matrix diagonal blocks corresponds to the metrological box where the photoresist grating structure is. The incidence and azimuthal angles are fixed at $\theta = 60°$ and $\phi = 0°$, respectively.

Table II presents the comparison of fitting parameters obtained from SEM and MMIE measurements, of which the MMIE-measured results were extracted from Mueller matrix spectra collected by a single pixel located near the center of the metrological box. In other word, the MMIE-measured results are equivalent to those obtained by a MME with a beam size of about 5.86×5.86 μm^2, which is much smaller than microspot sizes in current scatterometry techniques (typically between 50 and 25 μm). In the data analysis, we just let the structural parameters $x_1 \sim x_4$ vary while other parameters were fixed at their nominal values. The standard deviations associated with the Mueller matrix elements $\sigma(m_{ij,k})$ in Eq. (12) were achieved based on the standard deviation of 30 repeated Mueller matrix measurements. In the solution of the inverse diffraction problem by the Levenberg-Marquardt algorithm, we took the nominal dimensions of the above four structural parameters as their initial values. According to Table II, we can observe that the MMIE-measured results exhibit good agreement with those measured by SEM. Figure 6 shows the fitting result of the measured and calculated best-fit Mueller

TABLE II. Comparison of fitting parameters of the photoresist grating structure extracted from MMIE and SEM measurements. The MMIE-measured values include 95% confidence limits and the SEM-measured values include estimate for errors in manually measuring the SEM micrographs.

Parameter	Nominal value	MMIE[a]	SEM
x_1 (nm)	200	203.8 ± 1.7	203.4 ± 4.9
x_2 (deg)	90	89.2 ± 0.2	89.5 ± 0.3
x_3 (nm)	311	309.6 ± 0.9	303.7 ± 6.8
x_4 (nm)	115	117.7 ± 0.5	111.3 ± 4.1

[a]The results were extracted from Mueller matrices collected by a single pixel of the camera.

Reuse of AIP Publishing content is subject to the terms at: https://publishing.aip.org/authors/rights-and-permissions. Download to IP: 115.156.193.89 On: Wed, 15 Jun 2016 09:24:26

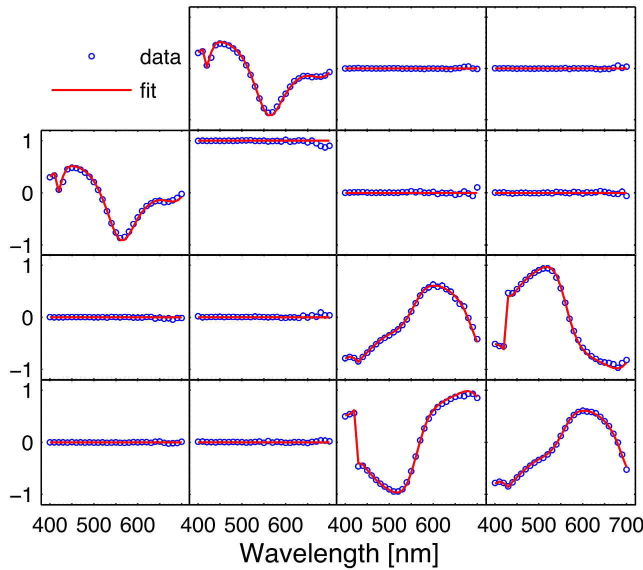

FIG. 6. Fitting result of the calculated best-fit Mueller matrix spectra and the measured spectra collected by a single pixel of the MMIE camera. The wavelengths are varied from 400 to 700 nm with increments of 10 nm. The incidence and azimuthal angles are fixed at $\theta = 60°$ and $\phi = 0°$, respectively.

matrix spectra. A good agreement can also be observed from Fig. 6, which yields a fitting error of $\chi_r^2 = 11.76$.

We calculated the depolarization index spectrum associated with the MMIE-measured data by $DI = \sqrt{[\mathrm{Tr}(\mathbf{MM}^{\mathrm{T}}) - M_{11}^2]/3M_{11}^2}$, $0 \le DI \le 1$,[40] where $\mathrm{Tr}(\cdot)$ represents the matrix trace. $DI = 0$ and $DI = 1$ correspond to a totally depolarizing and a totally non-depolarizing Mueller matrix, respectively. The calculated depolarization indices indicate that $|DI - 1| < 0.082$ in the whole spectral range of 400–700 nm. The depolarization effect was thus ignored in the data analysis. We also let the incidence and azimuthal angles vary to examine their influence on the final fitting result. The achieved incidence and azimuthal angles as well as the fitting error are $\theta = 60.13° \pm 0.178°$, $\phi = -0.29° \pm 0.215°$, and $\chi_r^2 = 11.55$, respectively. It suggests that the increase of fitting parameters does not lead to noticeable improvement in the final fitting result. We thereby fixed the incidence and azimuthal angles in the data analysis. Additionally, for the single pixel data analysis presented in Table II, we can calculate that the illumination spot on the sample surface has a size of about 11.72×5.86 $\mu\mathrm{m}^2$ when the incidence angle $\theta = 60°$. According to this spot size, we further know that, the illumination spot corresponding to a single pixel of the camera covers at least 29 grating periods. It is thus sufficient for the reflected fields to approach plane waves,[41] as required in the RCWA calculation.

Besides the ellipsometric analysis performed for a single pixel, we can also perform parallel ellipsometric analysis for all the pixels of interest located in the metrological box to obtain the distribution of fitting parameters over a large area. Figure 7 presents the three-dimensional (3D) maps of structural parameters $x_1 \sim x_4$ as well as their uncertainties $u(x_1) \sim u(x_4)$ (with 95% confidence limits) of the photoresist grating structure over a whole metrological box. Figure 8 presents the 3D map of the corresponding fitting error of data analysis for the whole metrological box. In the analysis, we ignored 2 pixels located near the edges of the metrological box to make sure that the illumination spot corresponding to each analyzed pixel covers identical and enough grating periods for reflected fields to approach plane waves. The lateral resolution of Figs. 7 and 8 mainly depends on the pixel size of the camera, the image magnification of the imaging lens, as well as the incidence angle. For the developed instrument, the lateral resolution of Figs. 7 and 8 is 11.72 μm and 5.86 μm, respectively, in the parallel (X) and perpendicular (Y) direction with respect to the plane of incidence. It should be noted that here the lateral resolution of Figs. 7 and 8 is different from that of the instrument, as discussed at the end of Section II B. In fact, according to the spatial resolution of the present instrument, we can take each four adjacent pixels

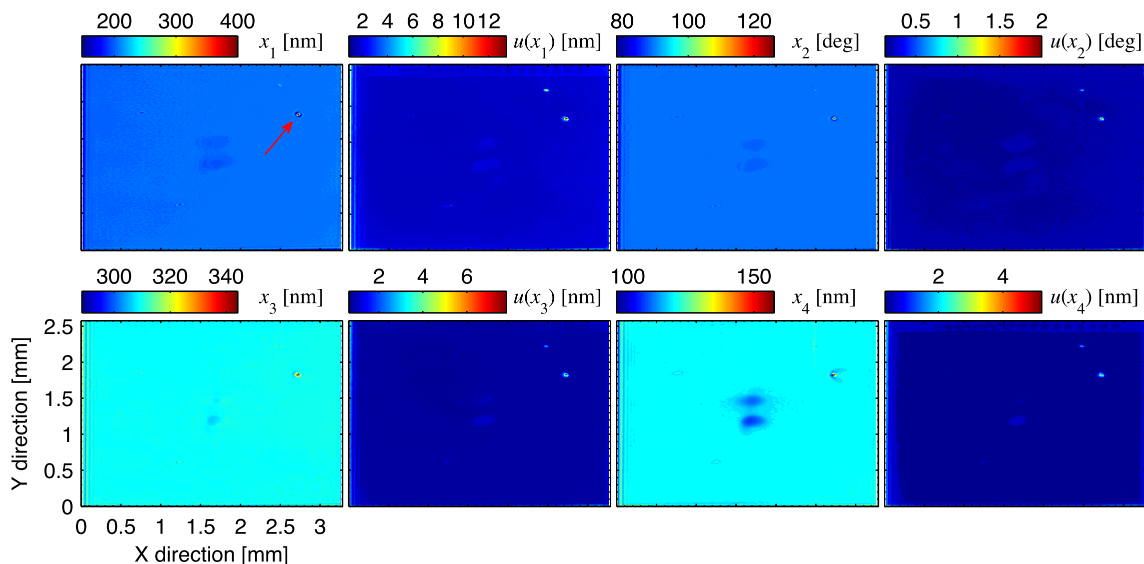

FIG. 7. Maps of the structural parameters $x_1 \sim x_4$ as well as their uncertainties $u(x_1) \sim u(x_4)$ (with 95% confidence limits) of the photoresist grating structure over the whole metrological box shown in Fig. 5. The grating period is along the X direction. Data were obtained by performing ellipsometric analysis for each pixel of the measured imaging Mueller matrices.

Reuse of AIP Publishing content is subject to the terms at: https://publishing.aip.org/authors/rights-and-permissions. Download to IP: 115.156.193.89 On: Wed, 15 Jun 2016 09:24:26

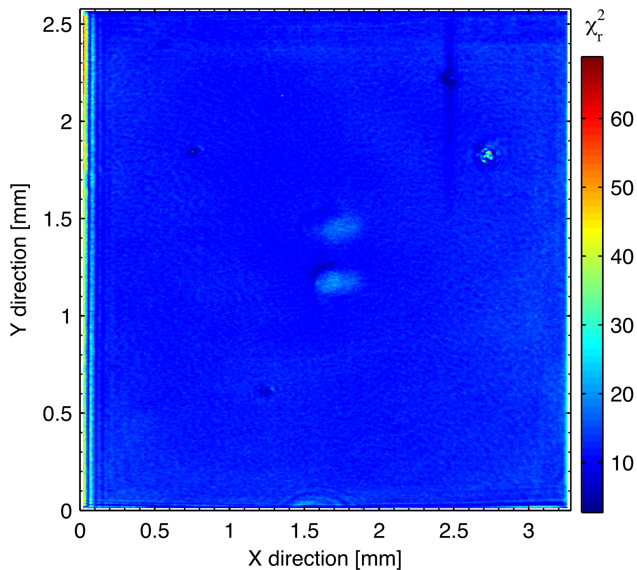

FIG. 8. Map of the fitting error χ_r^2 of data analysis for the whole metrological box shown in Fig. 5. Other settings of this figure are identical to those of Fig. 7.

as a group and then average the corresponding irradiances for further ellipsometric analysis to obtain the distribution of fitting parameters and meanwhile to improve the signal-to-noise ratio. Anyway, as can be observed from Fig. 7, the structural parameters exhibit relatively uniform variation and reasonable agreement with their nominal values as well as with the SEM-measured results given in Table II. Some exotic pixels (indicated by an arrow) are observed from the parameter maps, which show an extremely large deviation from the nominal parameter values. These exotic pixels can also be observed in the fitting error map given in Fig. 8 and in the imaging Mueller matrix presented in Fig. 5, which might be induced by unknown contaminants on the sample surface.

V. SUMMARY AND OUTLOOK

This work presents the development of a spectroscopic MMIE for nanostructure metrology. The developed instrument adopts a dual rotating-compensator configuration to collect the full 4×4 Mueller matrix in a single measurement. A regression method has been proposed to calibrate the system parameters. Some typical specifications of the instrument are summarized as follows. (1) Spectral range: 400–700 nm; (2) measurement time at a single wavelength: ~10 s; (3) image magnification: 1:1; (4) pixel size: 5.86×5.86 μm^2 (totally 1936×1216 pixels); (5) measurement accuracy and precision: less than 0.01 for all the Mueller matrix elements in both the whole image and the whole spectral range. The developed spectroscopic MMIE was then used to measure a photoresist grating sample in combination with an inverse diffraction problem solving technique. We have demonstrated its great capability in accurate nanostructure reconstruction from spectral data collected by a single pixel of the camera and for efficient quantification of geometrical profile of the nanostructure over a large area with pixel resolution. It is worth pointing out that the above-mentioned specifications of the present instrument are no fundamental limits. Future work will further broaden the spectral range and reducing the measurement time by choosing proper optical elements and increasing the intensity of light entering into the camera. In addition, the depolarization effect was ignored in the analysis of the photoresist grating sample due to the small depolarization indices in the measurement. However, it should be noted that the present technique is always applicable to a depolarizing sample. In the presence of depolarization, Eq. (11) cannot be applied to directly derive the Mueller matrix from the corresponding Jones matrix any more. Theoretical depolarizing Mueller matrices can be calculated by first transforming them into weighted sum of series of non-depolarizing Mueller matrices and then each non-depolarizing Mueller matrix is calculated by Eq. (11).[10] In the future, much more nanostructures will be measured to examine the great potential of MMIE.

ACKNOWLEDGMENTS

This work was funded by the National Natural Science Foundation of China (Grant Nos. 51475191, 51405172, 51575214, and 51525502), the Natural Science Foundation of Hubei Province of China (Grant No. 2015CFA005), the China Postdoctoral Science Foundation (Grant Nos. 2014M560607 and 2015T80791), and the Program for Changjiang Scholars and Innovative Research Team in University of China (Grant No. IRT13017). The authors would like to thank Shanghai Micro Electronics Equipment Co., Ltd. (Shanghai, China) for preparing the grating samples.

[1]R. M. A. Azzam and N. M. Bashara, *Ellipsometry and Polarized Light* (North-Holland, Netherland, 1977).
[2]H. Fujiwara, *Spectroscopic Ellipsometry: Principles and Applications* (Wiley, New York, 2007).
[3]X. Niu, N. Jakatdar, J. Bao, and C. Spanos, IEEE Trans. Semicond. Manuf. **14**, 97 (2001).
[4]H. T. Huang, W. Kong, and F. L. Terry, Jr., Appl. Phys. Lett. **78**, 3893 (2001).
[5]T. Novikova, A. De Martino, S. B. Hatit, and B. Drévillon, Appl. Opt. **45**, 3688 (2006).
[6]T. Novikova, A. De Martino, P. Bulkin, Q. Nguyen, and B. Drévillon, Opt. Express **15**, 2033 (2007).
[7]Y. N. Kim, J. S. Paek, S. Rabello, S. Lee, J. Hu, Z. Liu, Y. Hao, and W. McGahan, Opt. Express **17**, 21336 (2009).
[8]X. Chen, S. Liu, C. Zhang, and H. Jiang, J. Micro/Nanolithogr., MEMS, MOEMS **12**, 033013 (2013).
[9]X. Chen, C. Zhang, S. Liu, H. Jiang, Z. Ma, and Z. Xu, J. Appl. Phys. **116**, 194305 (2014).
[10]S. Liu, X. Chen, and C. Zhang, Thin Solid Films **584**, 176 (2015).
[11]M. Losurdo, M. Bergmair, G. Bruno, D. Cattelan, C. Cobet, A. De Martino, K. Fleischer, Z. D. Mitrovic, N. Esser, M. Galliet, R. Gajic, D. Hemzal, K. Hingerl, J. Humlicek, R. Ossikovski, Z. V. Popovic, and O. Saxl, J. Nanopart. Res. **11**, 1521 (2009).
[12]T. Mishima and K. C. Kao, Opt. Eng. **21**, 1074 (1982).
[13]R. F. Cohn, J. W. Wagner, and J. Kruger, Appl. Opt. **27**, 4664 (1988).
[14]M. Erman and J. B. Theeten, J. Appl. Phys. **60**, 859 (1986).
[15]D. Beaglehole, Rev. Sci. Instrum. **59**, 2557 (1988).
[16]G. Jin, R. Jansson, and H. Arwin, Rev. Sci. Instrum. **67**, 2930 (1996).
[17]B. L. Boulesteix, A. De Martino, B. Drévillon, and L. Schwartz, Appl. Opt. **43**, 2824 (2004).
[18]O. Arteaga, M. Baldrís, J. Antó, A. Canillas, E. Pascual, and E. Bertran, Appl. Opt. **53**, 2236 (2014).
[19]S. Liu, W. Du, X. Chen, H. Jiang, and C. Zhang, Opt. Express **23**, 17316 (2015).
[20]R. Reiter, H. Motschmann, H. Orendi, A. Nemetz, and W. Knoll, Langmuir **8**, 1784 (1992).

Reuse of AIP Publishing content is subject to the terms at: https://publishing.aip.org/authors/rights-and-permissions. Download to IP: 115.156.193.89 On: Wed, 15 Jun 2016 09:24:26

[21]A. Brechling, M. Pohl, U. Kleineberg, and U. Heinzmann, J. Biotechnol. **112**, 115 (2004).
[22]U. Wurstbauer, C. Röling, U. Wurstbauer, W. Wegscheider, M. Vaupel, P. H. Thiesen, and D. Weiss, Appl. Phys. Lett. **97**, 231901 (2010).
[23]A. Shan, M. Fried, G. Juhász, C. Major, O. Polgár, Á. Németh, P. Petrik, L. R. Dahal, J. Chen, Z. Huang, N. J. Podraza, and R. W. Collins, IEEE J. Photovoltaics **4**, 355 (2014).
[24]K. M. Twietmeyer, R. A. Chipman, A. E. Elsner, Y. Zhao, and D. VanNasdale, Opt. Express **16**, 21339 (2008).
[25]T. Novikova, A. Pierangelo, S. Manhas, A. Benali, P. Validire, B. Gayet, and A. De Martino, Appl. Phys. Lett. **102**, 241103 (2013).
[26]A. Pierangelo, S. Manhas, A. Benali, C. Fallet, J.-L. Totobenazara, M.-R. Antonelli, T. Novikova, B. Gayet, A. De Martino, and P. Validire, J. Biomed. Opt. **18**, 046014 (2013).
[27]J. Li, B. Ramanujam, and R. W. Collins, Thin Solid Films **519**, 2725 (2011).
[28]R. A. Horn and C. R. Johnson, *Matrix Analysis* (Cambridge University Press, Cambridge, 1985).
[29]H. Gu, S. Liu, X. Chen, and C. Zhang, Appl. Opt. **54**, 684 (2015).
[30]J. R. Parker, *Algorithms for Image Processing and Computer Vision*, 2nd ed. (Wiley, New York, 2011).
[31]W. H. Press, S. A. Teukolsky, W. T. Vetterling, and B. P. Flannery, *Numerical Recipes: The Art of Scientific Computing*, 3rd ed. (Cambridge University Press, Cambridge, 2007).
[32]M. G. Moharam, E. B. Grann, D. A. Pommet, and T. K. Gaylord, J. Opt. Soc. Am. A **12**, 1068 (1995).
[33]L. Li, J. Opt. Soc. Am. A **13**, 1870 (1996).
[34]S. Liu, Y. Ma, X. Chen, and C. Zhang, Opt. Eng. **51**, 081504 (2012).
[35]X. Chen, S. Liu, H. Gu, and C. Zhang, Thin Solid Films **571**, 653 (2014).
[36]X. Chen, S. Liu, C. Zhang, and H. Jiang, Appl. Opt. **52**, 6726 (2013).
[37]C. H. Herzinger, B. Johs, W. A. McGahan, J. W. Woollam, and W. Paulson, J. Appl. Phys. **83**, 3323 (1998).
[38]A. R. Forouhi and I. Bloomer, Phys. Rev. B **38**, 1865 (1988).
[39]G. E. Jellison, Jr. and F. A. Modine, Appl. Phys. Lett. **69**, 371 (1996).
[40]J. J. Gil and E. Bernabeu, Opt. Acta **33**, 185 (1986).
[41]R. M. Silver, T. A. Germer, R. Attota, B. M. Barnes, B. Bunday, J. Allgair, E. Marx, and J. Jun, Proc. SPIE **6518**, 65180U (2007).

Reuse of AIP Publishing content is subject to the terms at: https://publishing.aip.org/authors/rights-and-permissions. Download to IP: 115.156.193.89 On: Wed, 15 Jun 2016 09:24:26